ChemPhysChem

Research Article
doi.org/10.1002/cphc.202200906

Chemistry Europe
European Chemical Societies Publishing

www.chemphyschem.org

Unraveling the Photophysical Characteristics, Aromaticity, and Stability of π–Extended Acene-Quinodimethyl Thioamides†

Guang Yang[+],[a] Young Ju Yun[+],[a] Francesca Peccati[+],[b] Abdelqader M. Jamhawi,[a] Nareshbabu Kamatham,[a] Steffen Jockusch,[c] Gonzalo Jiménez-Osés,*[b, d] and A. Jean-Luc Ayitou*[a]

Poly-aromatic systems that contain quinodimethyl (QDM) units are appealing for several photonic and spintronic applications owing to the unique electronic structure, aromaticity, and spin state(s) of the QDM ring. Herein, we report the synthesis and characterization of novel QDM-based chromophores **1**–**3**, which exhibit unique photo-excited behavior and aromaticity. Extending the aromatic core with a biphenyl/phenanthryl- and a pyrrolo-fragment led to reducing the optoelectronic bandgap and modulating the photophysics QDM **1**–**3**. Yet, QDM **2** and **3** suffer from "aromaticity imbalance" and become relatively unstable compared to the parent compound QDM **1**. Further assessment of local aromaticity using computational tools revealed that the pseudo-quinoidal ring B is the main driving force allowing to easily populate the excited triplet state of these chromophores. The present study provides complementary guidelines for designing novel non-classical poly-aromatic systems.

Introduction

The chemistry of quinodimethyl (QDM) containing molecular systems was first introduced by Thiele[1] and Chichibabin[2] at the beginning of the last century. Over a hundred years later, many esteemed researchers still debate the electronic structure, aromaticity, and spin configuration of QDM. Depending on the structural features of QDM-based systems, it has been documented that *para- or ortho*-QDM (*p*-QDM and *o*-QDM) motifs would exist as mixtures of two resonant structures (Figure 1).[3,4] Neutral π-conjugated hydrocarbons and heterocycles containing the QDM motifs have been extensively studied and documented in several eminent reports.[5,6] Although the corresponding open-shell benzenoid structures (from *p*- and *o*-QDM) are Hückel aromatic species, their radical/radicaloid nature could render compounds containing the QDM motif unstable at ambient conditions.

Nevertheless, despite the chimeric nature and attractive chemo-physical properties of the QDM compounds, many research groups have prepared tens of QDM derivatives[7–11] exhibiting various degrees of stability under ambient conditions. As a result, QDM-based molecular systems have been useful in applications that range from spintronics[12,13] and optoelectronics devices.[14–17] The diradicaloid species of QDM

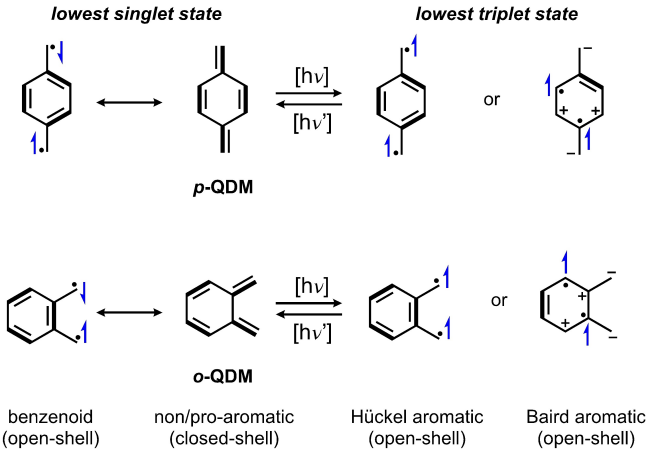

Figure 1. Resonant structures of *p*-QDM and *o*-QDM and their corresponding Hückel- and Baird-type species in the appropriate electronic/spin state(s). Adapted from Reference [4].

[a] G. Yang,[+] Dr. Y. J. Yun,[+] Dr. A. M. Jamhawi, Dr. N. Kamatham, Prof. A. J.-L. Ayitou
Department of Chemistry, University of Illinois at Chicago, Chicago, IL 60607, USA
E-mail: aayitou@uic.edu
Homepage: https://sites.google.com/view/ayitoulab

[b] Dr. F. Peccati,[+] Prof. G. Jiménez-Osés
Center for Cooperative Research in Biosciences (CIC bioGUNE), Basque Research and Technology Alliance (BRTA), Bizkaia Technology Park, Building 800, 48160 Derio, Spain
E-mail: gjoses@cicbiogune.es
Homepage: http://www.gonzalojimenezoses.com

[c] Dr. S. Jockusch
Department of Chemistry & Center for Photochemical Sciences, Bowling Green State University, Bowling Green, OH 43403, USA

[d] Prof. G. Jiménez-Osés
Ikerbasque, Basque Foundation for Science, 48013 Bilbao, Spain

[+] These authors have contributed equally to this work.

Supporting information for this article is available on the WWW under https://doi.org/10.1002/cphc.202200906

could be obtained upon photoexcitation, but these species may become relatively unstable under ambient conditions.

While the stability and reactivities of QDM motifs are the main hinders to creating/preparing (pro)aromatic quinoidal systems, their unique electronic structure, aromaticity, spin state, and attractive photophysical characteristics are still fueling the interest and curiosity of theoreticians and experimentalists to explore novel QDM containing systems which could be tailored for various applications (*vide supra*).

Since the introduction of QDMs in the year the 1900s, various methods have been employed to modulate the stability of the two resonant structures; specifically, π-conjugation or fusing/disguising the pro-aromatic QDM unit into the backbone of classical aromatic systems has allowed chemists to modulate the interconversion between the close-shell quinoidal and open-shell benzenoid structures. Previously, we introduced a new cycloaddition reaction using phosphine disulfide (or Lawesson Reagent) and π-acidic acene diimides such as naphthalene diimide (NDI) to create a *p*-naphthoquinodimethyl *bis*-thioamide (QDM **1**) which features a *pseudo*-quinoidal *ring B* (Figure 2).[18] QDM **1** was employed in several photon management applications,[19–21] triplet photochemistry,[22,23] and photometric sensing.[24] The highly unusual stability of QDM **1** and its attractive photophysical characteristics prompted us to investigate the corresponding derivatives QDM **2** and **3** with the expectation to rely on π-extension to modulate the photophysics and aromaticity of the novel QDM chromophores. Importantly, the biphenyl/phenanthryl-based QDM **2** was previously reported;[25] however, this chromophore exhibits a half-life of ca. 24 h when kept under ambient conditions. From our earlier investigation involving QDM **2**, we hypothesized the following: a) the additional biphenyl/phenanthryl moiety in QDM **2** would enhance local aromaticity (aromatic stabilization energy) forcing the *pseudo*-quinoidal *ring B* to re-aromatize or b) the proximity of the sulfur atom to biphenyl/phenanthryl ring would induce $_{Ar}$C–S coupling. Here, we refer to "enhanced local aromaticity" as either increased aromatic stabilization energy (ASE) or having additional Clar's sextet units fused to the pro-aromatic *ring B* in QDM **2** and **3**. To qualitatively identify the root cause of poor stability and/or high reactivity of π-extended derivatives of QDM **1**, we synthesized QDM **3** that features a pyrrole *ring D* (starting from the DBU-fused NDI precursor, See Supporting Information for the syntheses, Schemes S5 & S7). Expectedly, the moderate ASE provided by the pyrrole ring in QDM **3** would alleviate local aromaticity felt by *ring B* (as observed in QDM **2**) and prevent a plausible reaction between the anionic thiocarbonyl and the $_{Ar}$C–H bond, as hypothesized in the case of QDM **2**. In this report, we wish not only to report a comparative photophysical study of QDM **1**–**3**, including the nature and kinetic of their photo-excited state, but also the aromaticity-induced stability and reactivity of these chromophores. In our investigation, we employed a combination of advanced photophysical and EPR tools and computational modeling to establish the photophysics and aromaticity of the ground- and excited-state species of these chromophores.

Results and Discussion

UV-vis Absorption and Photoluminescence Spectroscopy

The UV-vis absorption spectra of all three QDM derivatives QDM **1**, **2**, and **3** are reported in Figure 3. The absorption profile of QDM **1** has λ_{max} = 451, whereas that of QDM **2** and **3** are red-shifted to λ_{max} = 459 and 461 nm, respectively. The observed bathochromic shifts are due to the additional π-conjugation that reduced the HOMO-LUMO gap (Supporting Information, Figure S27 and Table 1). Interestingly, the QDM compounds exhibit a similar vibronic progression of their main absorption band. Likewise, the fluorescence and phosphorescence spectra of QDM **2** and **3** showed similar vibronic features that resemble that of the parent QDM **1**.[18,25] The quantum yield (Φ_F) of fluorescence for QDM **2** and **3** are 10–15 times higher than that of the parent compound QDM **1**; this suggests that the additional aromatic unit(s) in QDM **2** and **3** facilitate a faster $S_1 \rightarrow S_0$ radiative decay over the expected $S_n \rightarrow T_1$ intersystem crossing (ISC), as observed in the case of QDM **1**. The phosphorescence spectrum of QDM **1** recorded at 77 K

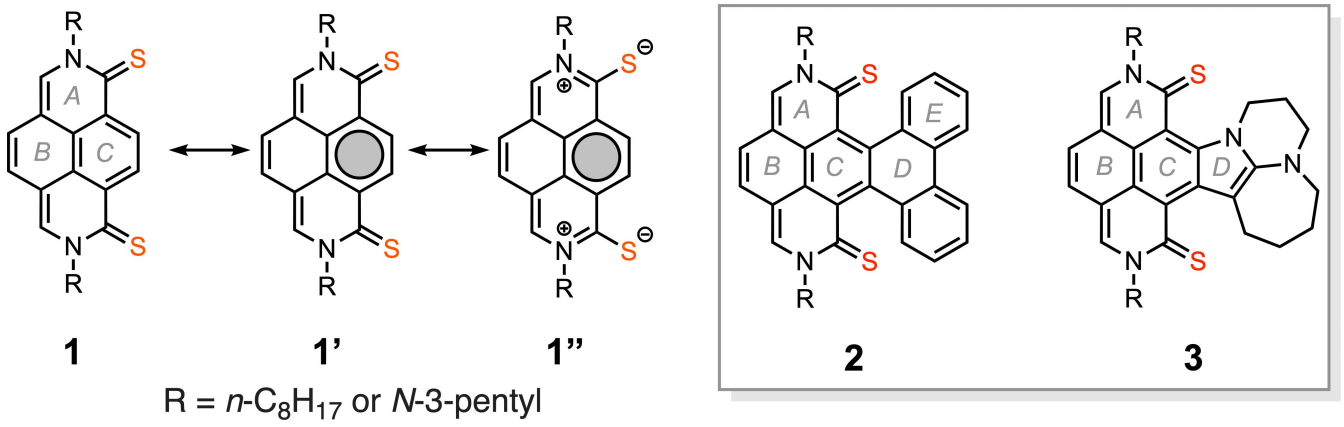

Figure 2. Chemical structures of QDM **1**, **2**, and **3**. The Kekulé and Clar structures of QDM **1** are also shown.

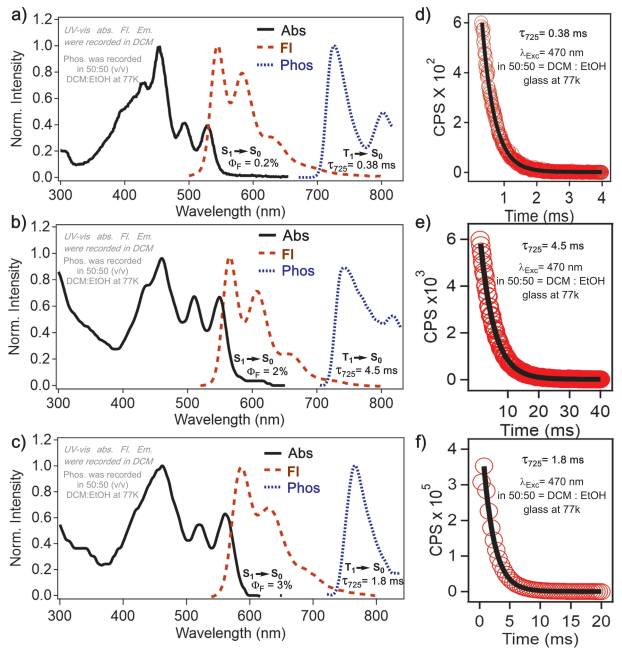

Figure 3. UV-vis absorption, steady state (fluorescence), and phosphorescence emission profiles were recorded in DCM and 50:50 DCM: EtOH glass at 77 K, respectively. QDM **1** (a), **2** (b), **3** (c) and d–e the corresponding phosphorescence decay kinetic (samples O.D. = 0.1 at λ_{Exc} = 470 nm).

in 1:1 ethanol/dichloromethane (EtOH/DCM) glassy matrix showed a band centered at 725 nm, whereas QDM **2** and **3** profiles are again red-shifted to 741 and 765 nm, respectively.

However, the phosphorescence lifetime of QDM **2** at 725 nm (τ_{phos} = 4.5 ms vs. 0.38 ms for QDM **1**) is the longest recorded in the series of QDM compounds (Figures 3d–e). The increase in phosphorescence lifetimes is likely due to the π-conjugation (biphenyl/phenanthryl-unit) that enhances local aromaticity in the excited state according to the Baird rule of aromaticity[26] in *ring B*. On the other hand, the trend in Φ_F and τ_P for QDM **2** and **3** indicates that π-extension likely induces rapid radiative deactivation of the singlet excited species but stabilizes the corresponding triplet species more than what was previously observed in the case of parent QDM **1**. Yet, the increase in resonance energy in QDM **2** and **3** is expected to contribute to the decrease of the rate of $S_n \rightarrow T_1$ ISC.

Transient Absorption Spectroscopy: To further explore the photo-behavior and kinetic of QDM **1**–**3**, we employed femtosecond (fs−) and nanosecond (ns−) transient absorption (TA) techniques to decipher the role of aromaticity and/or π-extension of the QDM of our interest. The TA spectra of QDM **1**–**3** were all recorded in degassed (Argon saturated) spectroscopy-grade DCM under room temperature in Figures 4 and 5. Within the probed range, the excited state ISC and singlet and triplet excited state absorption (ESA) bands can be observed in both fs- and ns-TA spectra. Upon photo-excitation of the three QDM at 470 nm, the ESA for the singlet transient ($S_1 \rightarrow S_n$) for the parent QDM **1** showed centered at ca. 520 and 780 nm, with a time constant of ca. 80 ps (Figure 3a–c). On the other hand, the singlet transients for QDM **2** and **3** appear at 650–790 nm with time constants of ca. 700 and 60 ps, respectively. It is worth noting that the ground state bleach and the ESA exhibit similar kinetic. Thus, we estimated the rate constant of ISC (k_{ISC}) to be 0.091×10^{10} s^{-1} for QDM **3**, 0.13×10^{10} s^{-1} for QDM **2**, and 1.3×10^{10} s^{-1} for QDM **1**. These estimates for k_{ISC} show that the $S_n \rightarrow T_1$ ISC for both QDM **2** and **3** is about one order of magnitude slower than the ISC process in QDM **1**, indicating that radiative decay $S_1 \rightarrow S_0$ is favored over the formation of triplet species of π-extended QDM **1**. This result also trends with the measured fluorescence quantum yields for QDM **2** and **3**.

From the fs-TA spectra, one can notice isosbestic features that indicate the ISC of the singlet transients to populate the triplet manifold of the three QDM compounds. As depicted in Figure 5, the triplet transient spectra match that of the bands that appear beyond the time constants associated with the lifetimes of the singlet transients. Figures 5a–c show the triplet transient spectrum of QDM **1** between 500–800 nm. A mono-exponential fit of the decay trace for this ESA gave a time constant of ca. 9 μs. Likewise, the triplet transient bands associated with the singlet ESA of QDM **2** and **3** appear in the same spectral range with noticeable ground state bleach at ca. 560 nm. The triplet transient lifetimes for these compounds were also fitted with a mono-exponential function to produce times constants of 180 ns and 3 μs, respectively.

To further ascertain that aromaticity extension would affect the stability of these QDM compounds, we performed stability studies of samples of QDM **2** and **3** illuminated with ambient light for 24–46 h using UV-vis and NMR techniques (Figure 6). It is worth noting that QDM **1** showed no sign of decomposition when exposed to air or kept under ambient light for months.[25] While it was found that QDM **2** and **3**

Table 1. Photophysical characteristics of QDM **1**–**3**.

	λ_{Abs} [a] [nm]	λ_{Fl} [a] [nm]	λ_{Phos} [b] [nm]	Φ_F [a,c] [%]	τ_{Phos} [d] [ms]	τ_{Phos} [d] [μs]	k_{ISC} [e] [s^{-1}]	$\Delta E_{L\text{-}H}$ [f] [eV]
1	451	543	725	0.2	0.38	8.7	1.3×10^{10}	3.27
2	459	564	741	2	4.5	0.18	0.13×10^{10}	3.01
3	461	584	765	3	1.8	3	0.091×10^{10}	2.82

[a] Recorded in spectroscopy grade and dry DCM. [b] Recorded in DCM: EtOH (v/v, 1:1) glassy matrix at 77 K. [c] QDM **1** was used as a standard to estimate the Φ_F for QDM **2** and **3**. [d] Laser power: maintained under 35 μW, λ_{exc} = 470 nm, all samples were recorded in degassed DCM. [e] The rate of intersystem crossing (ISC) was calculated from the lifetime of the singlet transient, $k_{ISC} = 1/\tau$ and approximating for the low Φ_F values. [f] Calculations were performed on abbreviated *N*-methylated models at the PBE0/cc-pVTZ level of theory (see Computational Details); $\Delta E_{L-H} = E_{LUMO} - E_{HOMO}$.

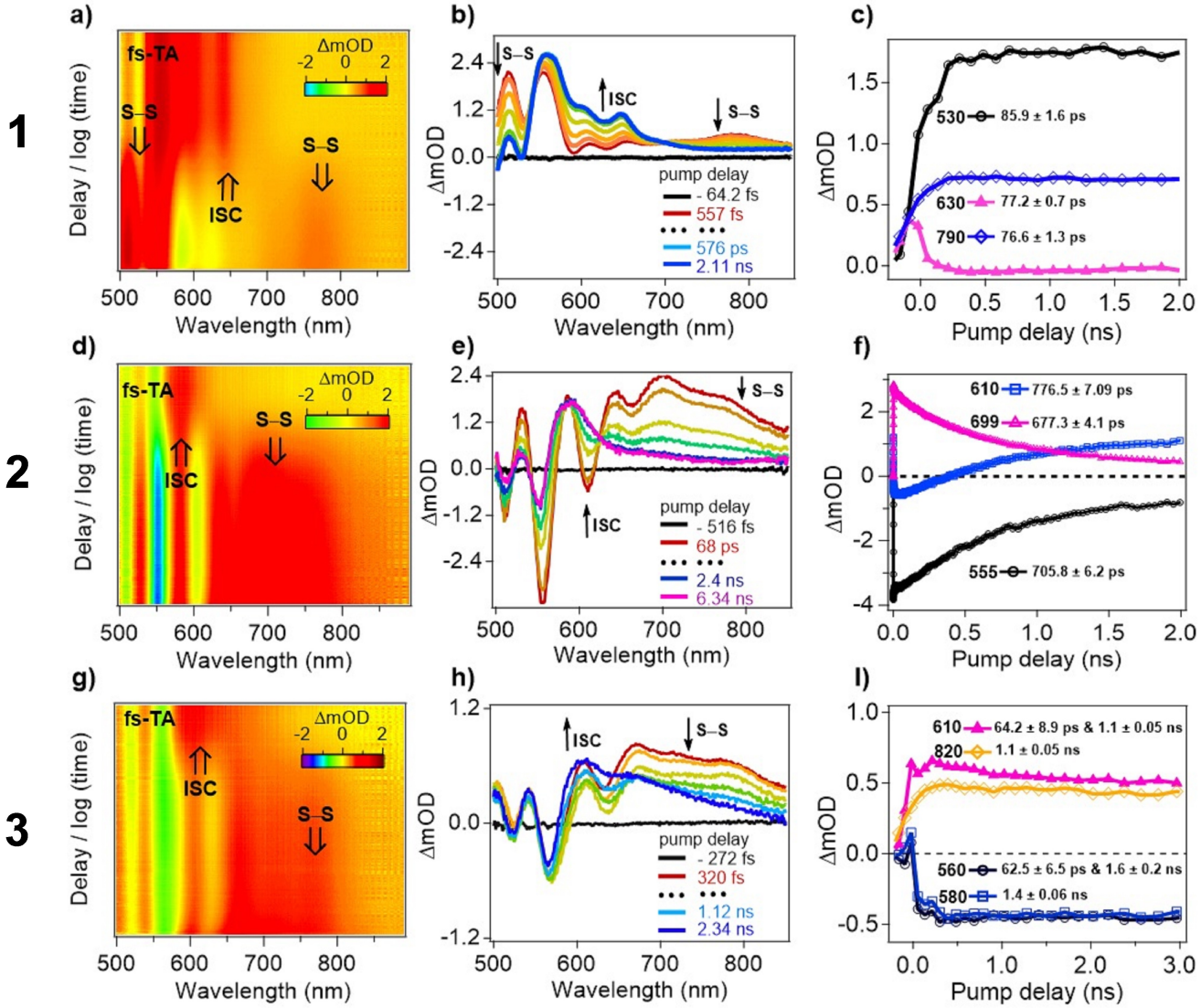

Figure 4. Femtosecond TA absorption spectra of QDM **1** (top), **2** (middle), and **3** (bottom). The samples were all prepared in dry and oxygen-free spectroscopy grade DCM (O.D. = 0.5–0.6), using a pump power of 35 μW at λ_{Exc} = 470 nm with a repetition rate of 2.1 kHz.

decompose when kept under ambient light (aerobic or anaerobic conditions), QDM **2** exhibits a higher degree of stability under both aerobic and anaerobic conditions compared to QDM **3** (Supporting Information, Figures S7 & S8). The observed dichotomy with QDM **2** and **3** prompted us to perform comparative stability studies while storing samples of these compounds under normal illumination and atmospheric conditions.

As illustrated in Figure 6a, for QDM **2**, the absorption spectrum showed a gradual disappearance of the vibronic bands with absorption maximum red-shifted. Similarly, for QDM **3**, the intensity of the absorption spectrum decreased within 46 h, and new broadband appeared between 600–700 nm (Figure 6b). The changes in the UV-vis spectra of QDM **2** and **3** suggest (photochemical) reactions; but when QDM **2** was kept in the dark for 96 h under aerobic and anaerobic conditions, no change was recorded in the UV-vis profile (Supporting Information, Figure S7). The appearance of new features in the two spectra with isosbestic points also indicates the formation of new species whose structures could be further elucidated using NMR or other spectroscopy techniques. In the partial ^{1}H NMR spectrum of QDM **2** (Figure 6c), the broadening of the NMR signals over 24 h was ascribed to the presence of an NMR inactive species or oligomeric/polymeric products. Compounds containing the *p*-quinoidal moiety are prone to undergo photochemical re-aromatization (*vide supra*). Furthermore, we postulated that the anionic sulfur atom in QDM **2**, could be reacting with the $_{Ar}$C–H of the biphenyl/phenanthryl synthon to form the NMR inactive species, as illustrated in Supporting Information, Figure S27a.

The scenario is different with QDM **3**, albeit the observed photo-bleaching. Because of an absence of the $_{Ar}$C–H in the vicinity of the thiocarbonyl group in QDM **3**, we ruled out the formation of the NMR inactive annulation by-product, as observed with QDM **2**. Instead, we postulated that *ring B* in QDM **2** most likely underwent re-aromatization; subsequently,

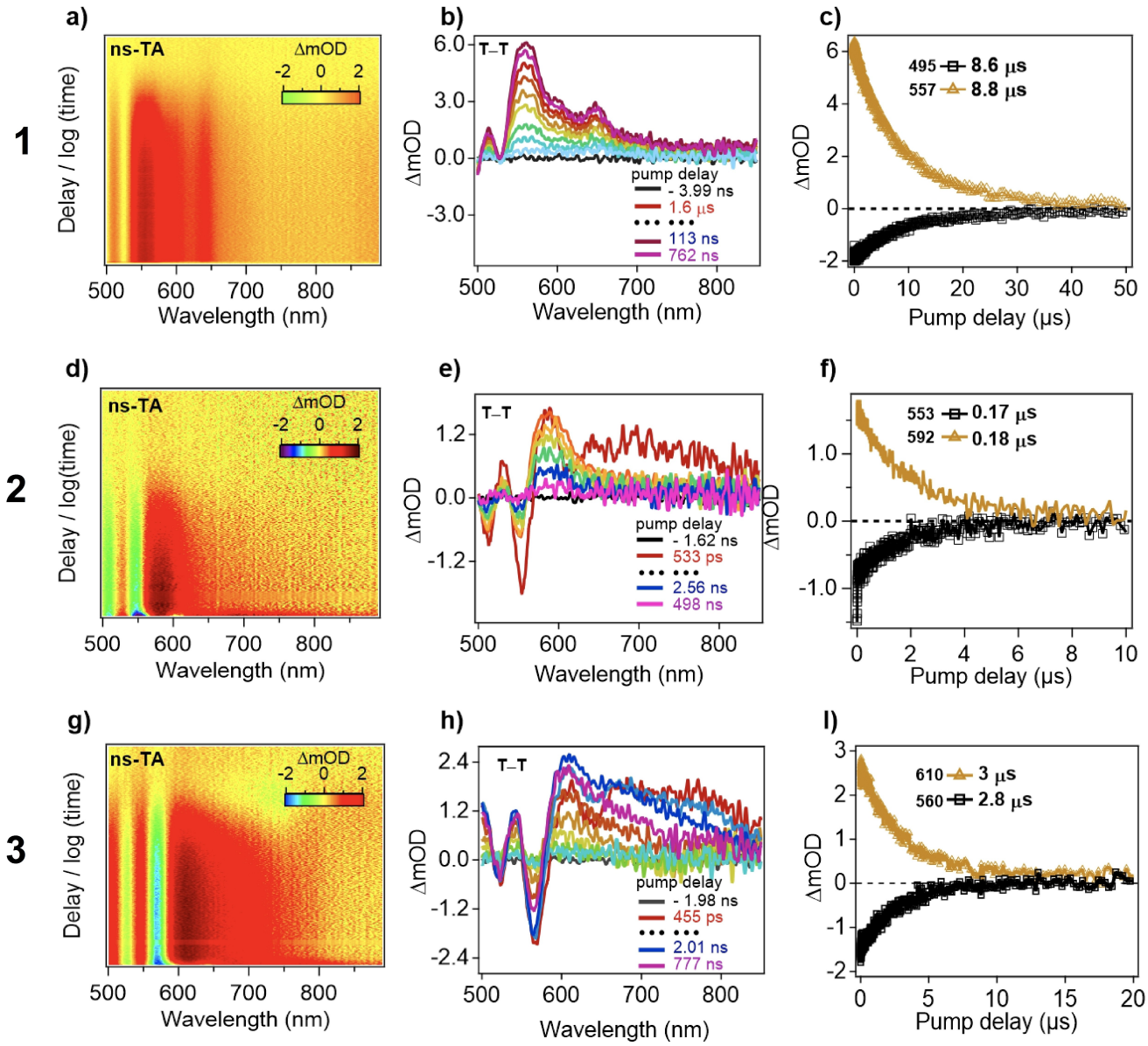

Figure 5. Nanosecond TA absorption spectra and kinetic for QDM **1** (top, a–c), **2** (middle, d–f), and **3** (bottom, g–i). The samples were all prepared in dry and oxygen-free spectroscopy grade DCM (O.D. = 0.5–0.6) and using a pump power of 35 μW at λ_{Exc} = 470 nm with a repetition rate of 1 kHz. T–T represents triplet-triplet absorption.

the reactive radicaloid species would quickly dimerize. This conjecture is confirmed by the appearance of a new NMR signal (doublet at δ 8.55 ppm) and new UV-vis absorption bands in the spectra of QDM **2** (Supporting Information, Figure S8).

Moreover, EPR spectroscopy experiments on samples of QDM **2** and **3** in the presence and absence of light and oxygen were recorded (Supporting Information, Figures S9–14). Accordingly, the EPR signals of the air-saturated and irradiated samples of QDM **3** showed 10 times increase in intensity compared to the signals of Argon-saturated samples (Supporting Information, Figure S11). The signals of the air-saturated and irradiated samples decreased in intensity when the light was turned off. After several cycles of irradiation-no irradiation (and aeration-deaeration), new features appeared in the original signals suggesting the presence of different types of radicals/radicaloid species, which react with oxygen through spin-spin interactions. The aromaticity extension and change in resonance of the QDM backbone (in **2** and **3**) might lead to forming these radicals or radicaloid species, thus compromising the stability of these chromophores regardless of the size/nature of the extended aromatic synthon.

Computational Investigations: Computational approaches were used to assess the impact of additional π-conjugation and how it affects both the energy of the frontier molecular orbitals and the intrinsic aromaticity (see Computational Details). As illustrated in Figure 7, the orbitals of QDM **2** and **3** share similar features. The difference in orbitals' shape

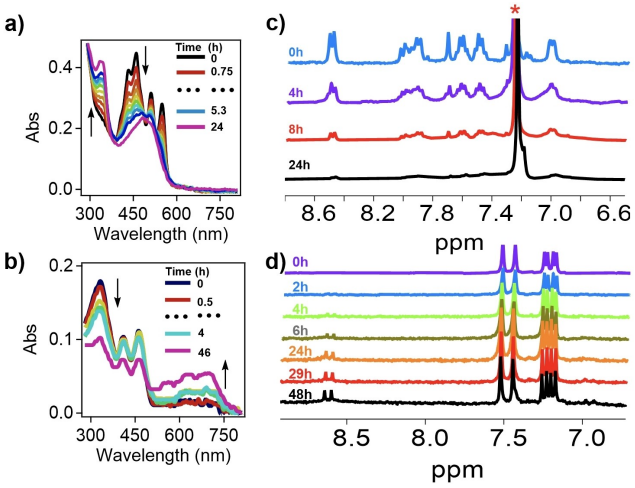

Figure 6. UV-vis absorption spectra of QDM **2** (a) and **3** (b) were recorded at various times in DCM while the samples were kept under ambient light. Partial ^{1}H NMR spectra of QDM **2** (c) in $CDCl_3$ and **3** (d) in CD_2Cl_2 at various times while the NMR tube was kept at ambient conditions.

observed in QDM **3** is likely due to the sp^3-hybridized atoms in the 6- and 7-membered rings. While there is no clear trend concerning the energy levels of the orbitals, it is noticeable that the HOMO-LUMO energy gap in QDM **2** and **3** has shrunk from 3.18 eV (QDM **1**) to 2.82 eV (QDM **3**). This agrees with the bathochromic shift observed in the corresponding UV-vis absorption and emission profiles. While the π-extension is expected to cause a reduction of the bandgap in QDM **2** and **3**, it was surprising to observe that adding a simple pyrrole ring could compromise the stability of QDM **1**.

The three QDM can be described as globally Hückel aromatic compounds; however, assessment of the local aromaticity of individual rings in these structures could clarify the role of *ring B* in dictating the photo-behaviors of QDM **1**–**3**. A comparison of aromaticity characters in individual rings was performed using NICS and HOMA calculations and analyzing paratropic and diatropic ring currents of all three QDM (Figure 8 and Supporting Information Figures S15–S21). On the ACID isosurface plots, one could observe diatropic ring currents moving around the individual rings in QDM **1**–**3**. However, the orientation of the density vectors around *ring B*

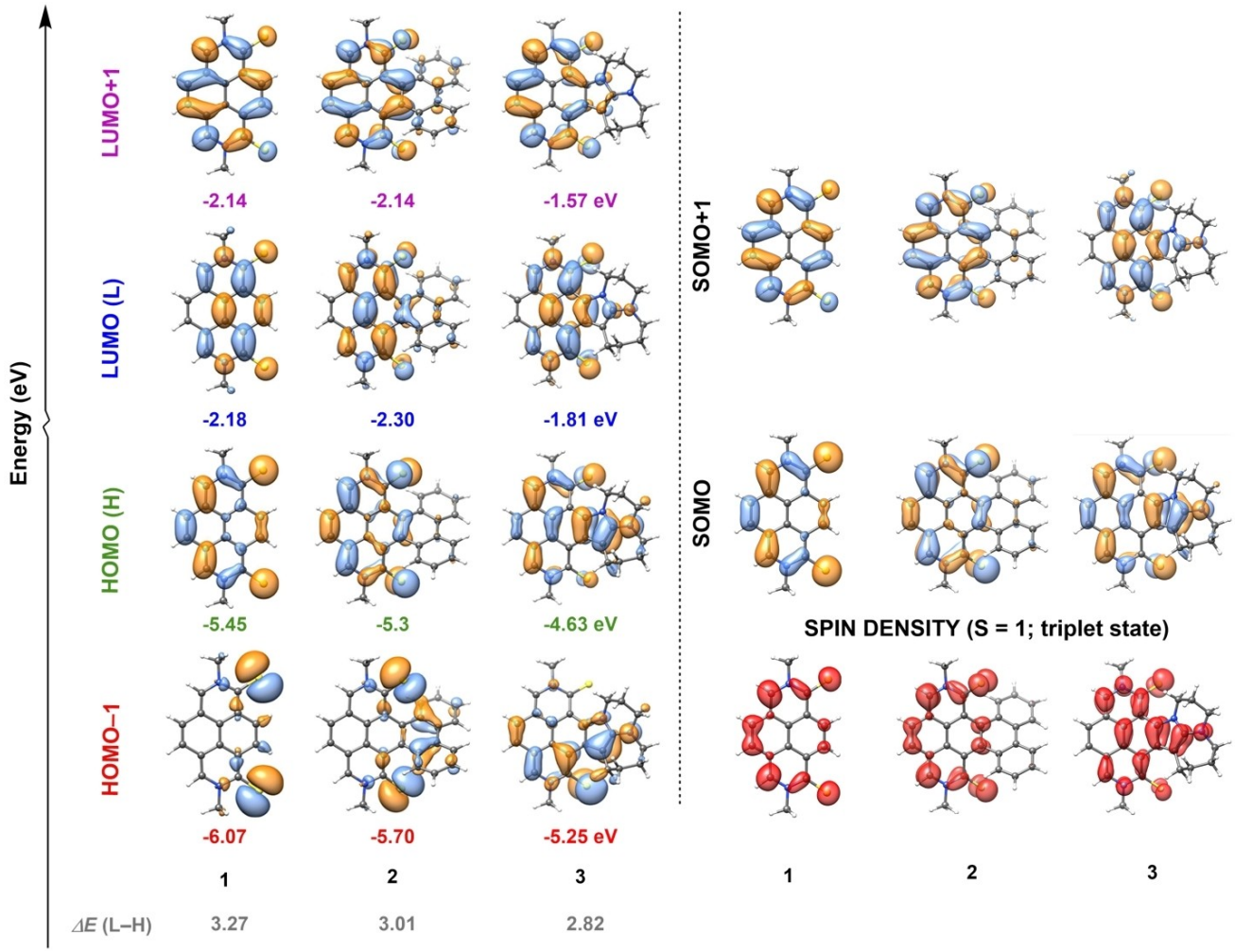

Figure 7. Frontier molecular orbital isosurfaces (plotted at isovalues −0.03 and 0.03) and energies in the singlet (*left*) and triplet (*right*) states. The latter is accompanied by spin density isosurfaces (plotted at an isovalue of 0.003) of QDM **1**–**3**. Calculations were performed using geometries optimized with PBE0/cc-pVTZ, $\Delta E_{L-H} = E_{LUMO} - E_{HOMO}$.

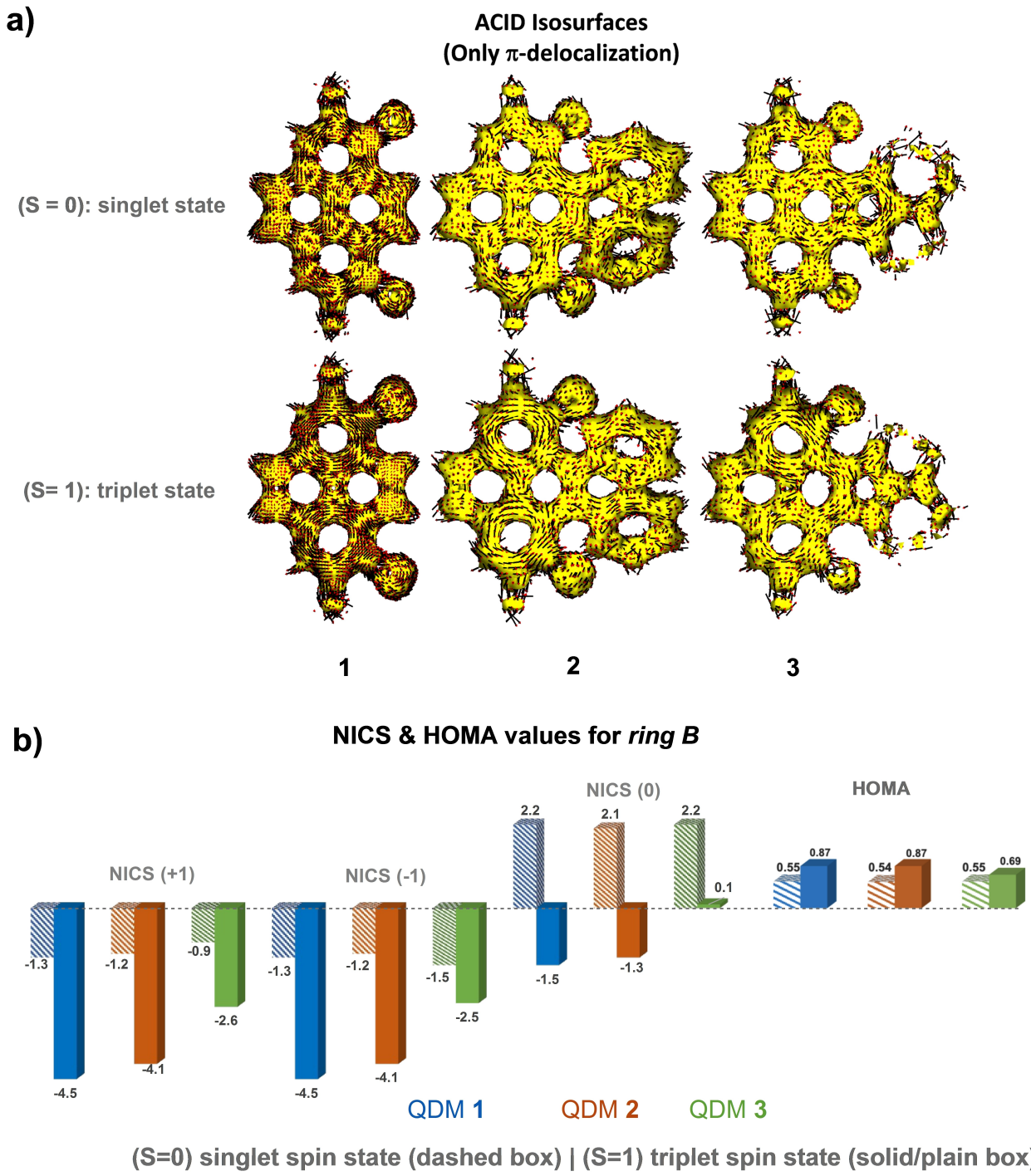

Figure 8. a) ACID isosurface plots (isovalue 0.026) of QDM **1**–**3**. Current density vectors are plotted onto the ACID isosurface to indicate dia– (aromatic, clockwise) and para–tropic (anti-aromatic, counterclockwise) ring currents. The applied magnetic field direction is perpendicular to the molecular and pointed outward. b) NICS(±1)/(0) and HOMA values for individual *ring B* (only) in QDM **1** (left), **2** (middle), and **3** (right). ACID, NICS, and HOMA calculations were performed at the HF/6-31 + G(d)//PBE0/cc-pVTZ level of theory (see Computational Details and Supporting Information Figures S15–S21 for further details including results at the CAM-B3LYP/6-31 + G(d)//PBE0/cc-pVTZ level).

is ambiguous, suggesting that the behavior of the ring is influenced/induced by local aromaticity from the neighboring rings. Likewise, in the triplet spin state, the direction of the ring currents seems to change from clockwise to counter-clockwise, indicating a reversal of aromaticity characters.

We previously proposed that local aromaticity in *ring B* is the driving force that populates the triplet manifold of QDM **1** excited species.[18,25] *Ring B* in all three QDM compounds can be regarded as a pseudo-quinoidal moiety that would exhibit minor Baird aromaticity or aromaticity reversal. With this in mind, one would expect an enhancement of local aromaticity

character in *ring B*. NICS(1)$_{zz}$ and NICS(0) calculations (Figure 8a) do indeed show that the characteristic of *ring B* changed from non-aromatic (in the singlet spin state) to aromatic (in the triplet spin state), although the increase in aromaticity upon singlet-to-triplet excitation is significantly smaller in pyrrole-functionalized QDM **3**. This trend is even more clear upon inspection of the HOMA indexes of the fully optimized geometries (Figure 9 & Figures S22–S24). This result agrees with our expectation that *ring B*, although locally pro-aromatic, can exhibit enhanced aromaticity in the lowest triplet excited state of the QDM compounds investigated in this work.

Conclusions

In summary, the comparative study of the photophysics and aromaticity of QDM **1**–**3** showed that fusing additional aromatic fragments onto QDM **1** would help stabilize the corresponding photo-excited triplet species. Still, the chemo-physio nature of the pro-aromatic pseudo-quinoidal *ring B* in QDM **2** and **3** becomes compromised due to enhanced local aromaticity and ASE. Further computational investigations revealed that local aromaticity in *ring B* is the main driving force allowing to easily populate the photo-excited triplet manifolds of the three QDM compounds. Although NICS calculations revealed that aromaticity is enhanced in *ring B* of these compounds in the triplet spins state, (photo)stability experiments show enhanced ASE due to aromaticity/π-extension in QDM **2** and **3** not only compromises the stability of these chromophores but also delays the $S_n \rightarrow T_1$ ISC process up to one order of magnitude compared to values obtained in the case of QDM **1**. The present study provides exciting results that allow us to explain the photophysical behaviors and stability of compounds containing pro-aromatic QDM motifs by the influence of local and global aromaticity.

Experimental Section

The synthetic procedures of QDM **1**–**3** are thoroughly described in the Supporting Information (Supporting Information, Schemes S1–S7). The target compounds were fully characterized by ^{1}H and ^{13}C NMR, FTIR spectroscopy, and Mass spectrometry. All commercially obtained reagents and solvents were used directly without further purification. UV-vis absorption spectra were recorded on an Ocean Optics spectrometer (DH-MINI UV-VIS-NIR Light Source and QE-Pro detector using Ocean View software package). Emission spectra were recorded on an Edinburgh Instrument FLS1000 spectrometer. Spectroscopy-grade dichloromethane (DCM) and ethanol (EtOH) solvents were used for all photophysical measurements.

Femtosecond and Nanosecond Transient Absorption Spectroscopy: Transient absorption spectroscopy was carried out using an integrated Helios and EOS experimental apparatus from Ultrafast Systems. The apparatus utilizes a Ytterbium Femtosecond Laser (Hyperion, Ultrafast Systems) with a fundamental at 1030 nm, a pulse duration ~290 fs, and repetition rates of 2.14 kHz for the femtosecond experiments and 1.0 kHz for the nanosecond experiments. The pump beam was generated using a three-stage optical parametric amplifier (Apollo-Y, Ultrafast systems) with pulse duration ranges from 100–400 fs. The femtosecond broadband probe extending between 360 and 500 nm was generated using the second harmonic of the Hyperion at 515 nm in a thin Sapphire plate. A second broadband probe extending between 500 and 910 nm was generated using the laser fundamental, 1030 nm, in a 1 cm Sapphire plate. Probe beams were steered through a Smart Delay Line (Ultrafast Systems) to scan the time domain with a delay window of ~7.5 ns and a minimum step size of ~3 fs. The nanosecond probe was generated using a separate supercontinuum laser (MOPA-based, Ultrafast Systems) with a pulse duration of ~0.75 ns. The pump-probe delay was generated electronically in the nanosecond transient absorption experiments. All probes were split into two separate beams. One of which was steered directly onto the reference detector and the other was steered through the sample compartment onto the signal detector. All samples were pumped with <85 nJ at 470 nm. Prior to the transient absorption measurements, all samples were dissolved in Dichloromethane and the optical density was adjusted to 0.4–0.6 (at 470 nm) in a 2 mm path length quartz cuvette. The sample solutions were then degassed through a freeze-pump-thaw routine that was repeated a minimum of three times.

Computational Details: Full geometry optimizations were carried out with Gaussian 16[27] using the PBE0 functional (called PBE1PBE in Gaussian) and cc-pVTZ basis set[28,29] with ultrafine integration grids in the gas phase and the ground close-shell singlet and excited triplet electronic spin states. The possibility of different conformations was taken into account for all structures. All stationary points were characterized by a frequency analysis performed at the same level used in the geometry optimizations, from which thermal corrections were obtained at 298.15 K. The quasi-harmonic approximation reported by Truhlar *et al.* was used to replace the harmonic oscillator approximation for the calculation of the vibrational contribution to enthalpy and entropy. [30] Scaled frequencies were not considered. Gibbs energies (ΔG) were used for the discussion on the relative stabilities of the considered structures. The lowest energy conformer for each calculated stationary point was considered in the discussion. Frontier Molecular Orbital (FMO) and spin density calculations were performed on the optimized geometries at the same level of theory in the gas phase and the ground singlet and excited triplet electronic spin states. Nucleus-Independent Chemical Shift (NICS)[31] and Anisotropy of the Induced Current Density (ACID)[32] calculations were performed on the PBE0/cc-pVTZ optimized geometries at the *ab initio* HF/6-31+G(d) and long-range-corrected DFT CAM-B3LYP/6-31+G(d)[33] levels of theory in the gas phase and the ground close-shell singlet and excited triplet electronic spin states. NICS was calculated at the ring centroid [NICS(0)] or 1 Å out-of-plane in the positive or negative direction perpendicular to the ring centroid [NICS(+1)$_{zz}$ and NICS(−1)$_{zz}$, respectively] with Gaussian 16 and the Gauge-Including Atomic Orbital (GIAO) method.[34] ACID calculations were performed with Gaussian 09 and the Continuous Set of Gauge Transformations (CSGT) method[35] using the keyword IOp(10/93=1), and later processed with the AICD 2.0.0 program[36] using 100,000 integration points and an optimization level of 0.015. The harmonic oscillator model of aromaticity (HOMA)[37–39] indexes were calculated on the PBE0/cc-pVTZ optimized geometries using the following formula [Eqs. 1]:

$$HOMA = 1 - \frac{1}{n}[\alpha_{CC} \sum^{i} \left(R_{CC_{opt}} - R_{CC_i}\right)^2 + \alpha_{CN} \sum^{i} \left(R_{CN\_opt} - R_{CN\_i}\right)^2] \quad (1)$$

where n is the number of bonds taken into the summation, α is a normalization constant ($\alpha_{CC} = 257.7\ A^{-2}$ for C–C bonds and $\alpha_{CN} = 93.5\ A^{-2}$ for C–N bonds) fixed to give HOMA = 0 for a model non-aromatic system and HOMA = 1 for the system with all bond lengths equal to the optimal value R_{opt}, assumed to be realized for fully aromatic systems ($R_{opt} = 1.388$ for C–C bonds and $R_{opt} = 1.334$ for C–N bonds). Cartesian coordinates, electronic energies, entropies, enthalpies, Gibbs energies, and lowest frequencies of the calculated structures are available in the Supporting Information; all the computed structures can be obtained from authors upon request.

Supporting information summary

Additional references are cited within the Supporting Information.[18,25,40–42]

Within the supporting information, details of the synthetic procedures for all precursors QDM **1**, **2**, and **3**: ^{1}H and ^{13}C NMR spectra, additional UV-vis absorption spectra, emission spectra, and additional computational data are included.

Funding sources

National Science Foundation under a CAREER grant no. 2211296 Awarded to AJA.

Grant RTI2018-099592-B-C22 from the Agencia Estatal Investigacion of Spain (AEI) to G.J.O.

Notes

The authors declare no competing financial interests.

Acknowledgements

This material is based upon work supported by the National Science Foundation under a CAREER grant no. 2211296 awarded to AJA. GJO thanks the Agencia Estatal Investigacion of Spain for the generous support through the grant RTI2018-099592-B-C22. F. P. thanks the Ministerio de Economía y Competitividad for a Juan de la Cierva Incorporación (IJC2020-045506-I) research contract. The authors thank the University of Illinois Chicago for supporting this work.

Conflict of Interests

The authors declare no conflict of interest.

Data Availability Statement

The data that support the findings of this study are available in the supplementary material of this article.

Keywords: aromaticity reversal · organic dyes · quinoidal chromophores · transient absorption spectroscopy · triplet photochemistry

[1] J. Thiele, H. Balhorn, *Ber. Dtsch. Chem. Ges.* **1904**, *37*, 1463–1470.
[2] A. E. Tschitschibabin, *Ber. Dtsch. Chem. Ges.* **1907**, *40*, 1810–1819.
[3] J. Casado, *Top. Curr. Chem.* **2017**, *375*, 73.
[4] S. Escayola, C. Tonnelé, E. Matito, A. Poater, H. Ottosson, M. Solà, D. Casanova, *Angew. Chem. Int. Ed.* **2021**, *60*, 10255–10265.
[5] Z. Zeng, X. Shi, C. Chi, J. T. L. Navarrete, J. Casado, J. Wu, *Chem. Soc. Rev.* **2015**, *44*, 6578–6596.
[6] J. Casado, R. P. Ortiz, J. T. L., *Chem. Soc. Rev.* **2012**, *41*, 5672–5686.
[7] P. Hu, S. Lee, T. S. Herng, N. Aratani, T. P. Gonçalves, Q. Qi, X. Shi, H. Yamada, K.-W. Huang, J. Ding, D. Kim, J. Wu, *J. Am. Chem. Soc.* **2016**, *138*, 1065–1077.
[8] A. Mahata, S. Chandra, A. Maiti, D. K. Rao, C. B. Yildiz, B. Sarkar, A. Jana, *Org. Lett.* **2020**, *22*, 8332–8336.
[9] B. Yang, S. Gao, *Chem. Soc. Rev.* **2018**, *47*, 7926–7953.
[10] B. Siret, S. Albrecht, A. Defoin, *C. R. Chim.* **2014**, *17*, 1075–1079.
[11] J. R. Wiseman, N. I. French, R. K. Hallmark, K. G. Chiong, *Tetrahedron Lett.* **1978**, *19*, 3765–3768.
[12] S. Shi, Z. Sun, X. Liu, A. Bedoya-Pinto, P. Graziosi, H. Yu, W. Li, G. Liu, L. Hueso, V. A. Dediu, M. Fahlman, *Adv. Electron. Mater.* **2018**, *4*, 1800077.
[13] Z. Sun, Z. Zeng, J. Wu, *Acc. Chem. Res.* **2014**, *47*, 2582–2591.
[14] T.-C. Tseng, C. Urban, Y. Wang, R. Otero, S. L. Tait, M. Alcamí, D. Écija, M. Trelka, J. M. Gallego, N. Lin, M. Konuma, U. Starke, A. Nefedov, A. Langner, C. Wöll, M. A. Herranz, F. Martín, N. Martín, K. Kern, R. Miranda, *Nat. Chem.* **2010**, *2*, 374–379.
[15] W. Chen, Q. Zhang, T. Salim, S. A. Ekahana, X. Wan, T. C. Sum, Y. M. Lam, A. H. H. Cheng, Y. Chen, Q. Zhang, *Tetrahedron.* **2014**, *70*, 6217–6221.
[16] J. Tang, Y. Gong, *J. Phys. Conf. Ser.* **2019**, *1298*, 012025.
[17] A.-K. Schönbein, J. Kind, C. M. Thiele, J. J. Michels, *Macromolecules* **2018**, *51*, 4678–4687.
[18] S. Shokri, J. Li, M. K. Manna, G. P. Wiederrecht, D. J. Gosztola, A. Ugrinov, S. Jockusch, A. Y. Rogachev, A. J.-L. Ayitou, *J. Org. Chem.* **2017**, *82*, 10167–10173.
[19] Y. J. Yun, N. Kamatham, M. K. Manna, J. Li, S. Liu, G. P. Wiederrecht, D. J. Gosztola, B. T. Diroll, A. Y. Rogachev, A. J.-L. Ayitou, *J. Phys. Chem. C.* **2020**, *124*, 12205–12212.
[20] S. Shokri, G. P. Wiederrecht, D. J. Gosztola, A. J.-L. Ayitou, *J. Phys. Chem. C.* **2017**, *121*, 23377–23382.
[21] M. K. Manna, S. Shokri, G. P. Wiederrecht, D. J. Gosztola, A. J.-L. Ayitou, *Chem. Commun.* **2018**, *54*, 5809–5818.
[22] J. Morgan, Y. J. Yun, A. J. Ayitou, *Photochem. Photobiol.* **2022**, *98*, 57–61.
[23] Y. J. Yun, F. Peccati, G. P. Wiederrecht, D. J. Gosztola, B. T. Diroll, G. Jiménez-Osés, A. J.-L. Ayitou, *J. Mater. Chem. C.* **2022**, *10*, 7093–7102.
[24] S. Maharjan, Y. J. Yun, V. A. Okello, G. P. Wiederrecht, D. J. Gosztola, A. J.-L. Ayitou, *J. Photochem. Photobiol. A* **2022**, *424*, 113648.
[25] N. Kamatham, J. Li, S. Shokri, G. Yang, S. Jockusch, A. Y. Rogachev, A. J. Ayitou, *Eur. J. Org. Chem.* **2020**, *8*, 917–922.
[26] N. C. Baird, *J. Am. Chem. Soc.* **1972**, *94*, 4941–4948.
[27] Gaussian 16 (Revision C.01), M. J. Frisch, G. W. Trucks, H. B. Schlegel, G. E. Scuseria, M. A. Robb, J. R. Cheeseman, G. Scalmani, V. Barone, G. A. Petersson, H. Nakatsuji, X. Li, M. Caricato, A. V. Marenich, J. Bloino, B. G. Janesko, R. Gomperts, B. Mennucci, H. P. Hratchian, J. V. Ortiz, A. F. Izmaylov, J. L. Sonnenberg, Williams, F. Ding, F. Lipparini, F. Egidi, J. Goings, B. Peng, A. Petrone, T. Henderson, D. Ranasinghe, V. G. Zakrzewski, J. Gao, N. Rega, G. Zheng, W. Liang, M. Hada, M. Ehara, K. Toyota, R. Fukuda, J. Hasegawa, M. Ishida, T. Nakajima, Y. Honda, O. Kitao, H. Nakai, T. Vreven, K. Throssell, J. A. M. Jr, J. E. Peralta, F. Ogliaro, M. J. Bearpark, J. J. Heyd, E. N. Brothers, K. N. Kudin, V. N. Staroverov, T. A. Keith, R. Kobayashi, J. Normand, K. Raghavachari, A. P. Rendell, J. C. Burant, S. S. Iyengar, J. Tomasi, M. Cossi, J. M. Millam, M. Klene, C. Adamo, R. Cammi, J. W. Ochterski, R. L. Martin, K. Morokuma, O. Farkas, J. B. Foresman, D. J. Fox, *Gaussian, Inc., Wallingford CT*, **2019**.
[28] R. A. Kendall, T. H. Dunning, R. J. Harrison, *J. Chem. Phys.* **1992**, *96*, 6796–6806.
[29] T. H. Dunning, *J. Chem. Phys.* **1992**, *90*, 1007–1023.
[30] R. F. Ribeiro, A. V. Marenich, C. J. Cramer, D. G. Truhlar, *J. Phys. Chem. B* **2011**, *115*, 14556–14562.
[31] P. von R. Schleyer, C. Maerker, A. Dransfeld, H. Jiao, N. J. R. van E. Hommes, *J. Am. Chem. Soc.* **1996**, *118*, 6317–6318.

[32] D. Geuenich, K. Hess, F. Köhler, R. Herges, *Chem. Rev.* **2005**, *105*, 3758–3772.
[33] T. Yanai, D. P. Tew, N. C. Handy, *Chem. Phys. Lett.* **2004**, *393*, 51–57.
[34] K. Wolinski, J. F. Hinton, P. Pulay, *J. Am. Chem. Soc.* **1990**, *112*, 8251–8260.
[35] T. A. Keith, R. F. W. Bader, *Chem. Phys. Lett.* **1993**, *210*, 223–231.
[36] R. Herges, D. Geuenich, *J. Phys. Chem.* **2001**, *105*, 3214–3220.
[37] T. M. Krygowski, M. Cyrański, *Tetrahedron* **1996**, *52*, 1713–1722.
[38] M. Cyrański, T. M. Krygowski, *Tetrahedron* **1996**, *52*, 13795–13802.
[39] T. M. Krygowski, *J. Chem. Inf. Comput. Sci.* **1993**, *33*, 70–78.
[40] C. Zhou, Y. Li, Y. Zhao, J. Zhang, W. Yang, Y. Li, *Org. Lett.* **2011**, *13*, 292–295.
[41] R. Mishra, P. Panini, J. Sankar, *Org. Lett.* **2014**, *16*, 3994–3997.
[42] R. Regar, R. Mishra, P. K. Mondal, J. Sankar, *J. Org. Chem.* **2018**, *83*, 9547–9552.

Manuscript received: December 12, 2022
Revised manuscript received: July 31, 2023
Accepted manuscript online: August 7, 2023
Version of record online: September 19, 2023